Finocchio D., Barba S., Basili R. (2016). Slip rate depth distribution for active faults in Central Italy using numerical models. *Tectonophysics*, 687, 232-244, doi: 10.1016/j.tecto.2016.07.031.

Slip rate depth distribution for active faults in central Italy using numerical models

Debora Finocchio*, Salvatore Barba, Roberto Basili

Istituto Nazionale di Geofisica e Vulcanologia, Roma, Italy. E-mail addresses: (t, salvatore.barba@ingv.it, roberto.basili@ingv.it.

* Permanent address: Bury Street, M3 7DX, Manchester, UK.

Corresponding author: Roberto Basili, *Via Vigna Murata, 605, 00143, Roma, Italy*; e-mail: roberto.basili@ingv.it; phone: +39-0651860516.

Highlights

- Numerical models improve the appraisal of the slip rates in central Italy
- The model slip rates vary with depth and differ for each fault
- Mean slip rates are ~1.1 mm/yr for normal faults and ~0.2 mm/yr for thrust faults
- 100 years after a large earthquake, the Avezzano fault is half unlocked at depth

Abstract

Slip rate is a critical parameter for describing geologic and earthquake rates of known active faults. Although faults are inherently three-dimensional surfaces, the paucity of data allows for estimating only the slip rate at the ground surface and often only few values for an entire fault. These values are frequently assumed as proxies or as some average of slip rate at depth. Evidence of geological offset and single earthquake displacement, as well as mechanical requirements, show that fault slip varies significantly with depth. Slip rate should thus vary in a presumably similar way, yet these variations are rarely considered.

In this work, we tackle the determination of slip rate depth distributions by applying the finite element method on a 2D vertical section, with stratification and faults, across the central Apennines, Italy. In a first step, we perform a plane-stress analysis assuming visco-elasto-plastic rheology and then search throughout a large range of values to minimize the RMS deviation between the model and the interseismic GPS velocities. Using a parametric analysis, we assess the accuracy of the best model and the sensitivity of its parameters. In a second step, we unlock the faults and let the model simulate 10 kyr of deformation to estimate the fault long-term slip rates.

The overall average slip rate at depth is approximately 1.1 mm/yr for normal faults and 0.2 mm/yr for thrust faults. A maximum value of about 2 mm/yr characterizes the Avezzano fault that caused the 1915, Mw 6.9 earthquake. The slip rate depth distribution varies significantly from fault to fault and even between neighbouring faults, with maxima and minima located at different depths. We found uniform distributions only occasionally. We suggest that these findings can strongly influence the forecasting of cumulative earthquake depth distributions based on long-term fault slip rates.

Keywords:

slip rate; numerical model; fault; rheology; central Italy

Supplementary document

The supplementary document includes the histogram of RMS deviations calculated for all model parameter variations; diagrams showing the comparison between the best interseismic model and all other model trials by varying the material parameters, boundary conditions, and unlocked faults and detachments; strain plots of the interseismic model and the long-term slip rate model; and a table of slip rate depth distributions for all faults in all fault combinations.

Table of Contents

1 Introduction

Fault slip rate is a fundamental quantity in studies on rock mechanics, tectonics and geodynamics, and seismic hazards. In the latter, slip rate is used to predict earthquake rates of the major active faults. However, geologically-derived slip rate is often an elusive quantity because its estimation requires that both the amount and age of the offset features be known. In most field studies, one or a few data points are commonly accepted as representing some presumed average displacement along the fault strike, and the time component is often associated with significant uncertainties and may span considerably different time frames (i.e., from a few tens to hundreds of years in the historical record, to tens of thousands of years in paleoseismology, to millions of years in some geologic studies). Numerical models provide more comprehensive estimates of fault slip rates when an independent method that includes the overall deformation, both on- and off-fault strain, is necessary. Geological restoration algorithms (as the trishear, Hardy and Ford, 1997; Allmendinger, 1998) work well when the fault geometry and the embedding chronostratigraphic units are adequately known (e.g., Gold et al., 2006; Maesano et al., 2015). Conversely, finite-element modelling is especially advantageous when the rock mechanical and rheological properties are well known. Finite-element models may incorporate various degrees of complexity of the structure under study. For example, Bird (1989, 1999) developed the program SHELLS for modelling a two-layer crust and lithospheric mantle, incorporating faults, lithospheric and rheological characteristics, laterally varying thermal structure, and geodynamic boundary conditions. This approach has been already applied in various cases and tectonic settings (e.g., Geist and Andrew, 2000, for California strike-slip faults; Bird, 2009, for active faults in the western US; Kastelic and Carafa, 2012, for thrusts and strike-slip faults in the Dinarides). Finite element models with mechanical layering and variable rheology have also been used to reproduce the long-term regional state of stress and strain or the forces that act on faults (e.g., Vergne et al., 2001; Hsu et al., 2003; Chamlagain and Hayashi, 2005; Carafa and Barba, 2011; Trubienko et al., 2013; Carafa et al., 2015). In more general terms, two main strategies can be followed to determine fault slip rates through numerical models: 1) the amount of slip is imposed on the fault plane (e.g., Ward and Valensise 1996; Hardy and Ford, 1997; Wang et al., 2006), or 2) the fault under the drive of tectonic forces is left to slip freely (e.g., Cowie et al., 1993; Bird, 1999). In both cases, the correct amount of slip rate is found by fitting the model results to a given set of deformation data. Geologic field studies and numerical models often rely on deformation data collected from the ground surface or shallow geologic probing. Such slip rate determinations thus exploit the effect onto the free surface of the actual slip on the fault plane at depth. Therefore, those values are often assumed to be the same as, or the average of, the slip rate at depth. However, knowing the slip rate distribution at depth, rather than just its inferred average, can be useful for improving our understanding of Earth's crust behaviour and bettering our estimates of earthquake rates.

In this work, we use finite-element models to calculate the slip rate distribution at depth. To this end, we set up a 2D-cross-sectional multilayer finite-element model in the central Apennines, Italy. The Apennines is an example of a youthful extensional system that progressively overprints an older contractional belt. More specifically, the contractional fold-and-thrust system migrates toward the east and is replaced by extension to the west (Elter et al., 1975), and the contraction and extension systems coexist at short distances from one another (e.g., Negredo et al., 1999; Pondrelli et al., 2008). Among the numerous active normal and thrust faults in the central Apennines, several are deemed to be seismogenic (Figure 1), and a few of them have actually generated damaging earthquakes in the last century or so (e.g., Avezzano 1915, Mw 6.9; Colfiorito 1997, Mw 6; L'Aquila 2009, Mw 6.3 for normal faulting; Senigallia 1930, Mw 5.8; Porto San Giorgio 1987, Mw 5.1 for thrust faulting).

As regards normal faults, several attempts using geological field data provided vertical throw rates in the range of 0.1 to 1.0 mm/yr (e.g., Roberts et al., 2004; Papanikolaou et al., 2005) and slip rates in the range of 0.2 to 1.3 mm/yr (e.g., Benedetti et al., 2013) derived from exhumed bedrock fault scarps. Similar values were obtained from broader Quaternary geologic data on intermountain basins by Pizzi et al. (2002). A few higher slip rates were instead proposed from paleoseismic trenching, such as the 1.6 mm/yr for the Fucino fault (Michetti et al., 1996), and the 2.5 mm/yr for the Ovindoli-Pezza fault (Pantosti et al., 1996). All these estimates are based on surface data. The unwieldy relationships between the actual faults at depth and their surface expression during earthquakes (e.g., Bray et al., 1994) or the plasticity of the material and the effect of gravity loads (e.g., Albano et al., 2015) are rarely considered in these types of study. Such complexities were noted on the occasion of recent earthquakes in central Italy, for example, by Barba and Basili (2000) and Chiaraluce et al. (2003) for the Colfiorito earthquakes of 1997 and Bonini et al. (2014) for the L'Aquila earthquake of 2009. Based on analogue models, Bonini et al. (2015) also showed that the growth and evolution of normal faults in the presence of inherited discontinuities, such as the detachments and thrust faults in the Apennines, can largely deviate from the ideal behaviour in isotropic conditions. Apennine thrust faults provide examples of slip rates directly derived from crustal depth deformation data. Visini et al. (2010) provided bulk horizontal contractional rates of 0.09 to 0.31 mm/yr for the outer Apennines belt based on seismicity. Using numerical methods of geological section restoration, Maesano et al. (2013) and Bigi et al. (2013) provided estimates of very long-term (2-5 My) average slip rates of some coastal and offshore thrust faults in the range of 0.26 to 1.35 mm/yr and 0.15 to 2.62 mm/yr, respectively. However, all of them are depth-averaged values.

Considering this tectonic context and the scale of the problem to tackle, we made a selection of the main active faults in the region (Figure 1) and included them in the model with a simplified geometry. The faults cut through a specially designed geological section obtained by combining several publicly available geological data at the regional scale of the model. We initially established a first-order deformation pattern that allowed us to compute the long-term slip rate at depth for all the fault planes under the free-slip condition. We let gravity and tectonic forces deform the model, and then varied several model parameters and faults in order to fit the geodetically-derived velocity field. Using the best model found in the previous step and testing several faults combinations, we then calculated the long-term fault slip rate at depth. We concluded that slip rate can vary significantly with depth and that this variation can take different shapes among the faults. We also found, among the various possible solutions, that some faults move oppositely from their geologically defined kinematics. The resulting average slip-rate values for our preferred option with respect to geologically-derived slip rates are systematically higher for normal faults and lower for thrust faults.

2 Data and methods

In this study, we constructed a 2D multi-layered finite element deformation model that combines visco-elasto-plastic rheology, discontinuities (detachments and faults), and gravity (Figure 2). The model section was chosen to be parallel to the principal stress components as indicated by SHmax (e.g. Carafa and Barba, 2013) and axes of focal mechanisms (e.g. Pondrelli et al., 2011) in the area so that we could conduct plane-stress analysis, where the out-of-plane stress is zero. The model was used to simulate the interseismic deformation and to derive the long-term slip rate of the embedded faults. In both analyses, the model performance was established by comparing the model output in terms of velocity field at the free surface with a reference velocity field derived from geodetic data. Since the a priori information about the model properties at the needed scale is generally affected by significant uncertainties, we set up an initial model based on information derived from the literature and then performed a trial-and-error procedure and a parametric analysis to search for the model geometry and parameters of layers, presence and locking of discontinuities, and boundary conditions that best fit the reference velocity field in the interseismic period. Considering that all the faults included in the model are deemed to be active in the recent geological time, the best model then served as a reference for calculating the long-term slip rate at depth by unlocking all the faults. The epistemic uncertainty in the actual presence and activity of faults was explored by including different fault sets in the slip rate calculations. The numerical analysis was performed using the MSC/Marc-Mentat finite element suite (2013; MSC Software Corporation, http://www.mscsoftware.com/).

2.1 Reference geodetic velocity

For the surface horizontal velocity field in the study area, we adopted a solution based on GPS motion with respect to a fixed Eurasian frame (Devoti et al., 2011). The used GPS data span the period from 1998 to 2009, which includes the L'Aquila earthquake (April 6th, 2009). The coseismic and postseismic displacement components of this earthquake were modelled and corrected in the dataset by the GPS analysts, along with the evaluation of seasonal variations and changes in the station equipment (Devoti et al., 2011). These geodetic velocities thus represent the interseismic velocity field. We selected the horizontal velocities for our model from GPS stations located within a 200-km-wide swath along the model section (Figure 3a). The section-parallel component of the horizontal velocity is shown in Figure 4. The section-normal component of the horizontal velocity represent an out-of-plane motion that is not modelled here.

Given the lack of GPS data in the Adriatic offshore, to constrain the eastern sector of the velocity field we considered that the Adriatic domain is undergoing compression. This stress condition in the Adriatic domain is supported by the seismic moment tensors (Figure 3a): the extensional regime which dominates the western and the inner parts of the chain gives way to the contractional and transcurrent regimes toward the east (Frepoli and Amato, 1997; Pondrelli et al., 2008) as indicated by a few compressive earthquakes generated in the Apennines northeast-verging thrusts (such as those of Senigallia, 1930, Mw 5.6, described by Vannoli et al., 2015, and Porto San Giorgio, 1987, Mw 5.1, described by Riguzzi et al., 1989) and a few caused by Dinarides southwest-verging thrusts (as the Jabuka Island, 2003, Mw 5.5, described by Herak et al., 2005, along with few other smaller compressive earthquakes). All these earthquakes have a roughly NE-SW trending compressive axis. We thus fixed a point at approximately 30 km to the northeast of the model section (to include the Apennines and Dinarides thrusts facing off against each other) as a zero-velocity reference (Figure 3b) and then interpolated the velocity data through an asymmetric double-sigmoid function, via robust weighting of residuals, and resampled the profile at a 1-km spacing to construct the horizontal velocity curve and the associated 95% confidence interval (Figure 4).

From SW to NE, three main sectors can be outlined: 1) 0-110 km; 2) 110-150 km; 3) 150-200 km. The first sector is dominated by extension. The velocity curve indicates low rates in the southwestern part and higher rates, peaking at almost 3.0 mm/yr, toward the northeast. The largest extension occurs in the steeper gradient zone at approximately 80 km. The second sector is characterized by a transition from extension to contraction. This change takes place where the velocity is highest but starts decreasing, and where the associated confidence interval is still rather narrow. The third sector includes the part of the velocity curve that is constrained to satisfy the null velocity at the outer thrust front. Here the velocity tapers to 0.3 mm/yr toward the model eastern edge. Notice that in this region, the confidence interval enlarges dramatically because the interpolated velocity is not directly derived from GPS data.

2.2 Numerical model setup

2.2.1 Model geometry

To draw the geological layers that make up the numerical model geometry (Figure 2), we used the geological interpretations of CROP-11, a 256-km-long deep seismic line across the central Apennines (Figure 1), from Patacca et al. (2008) and Di Luzio et al. (2009). Patacca et al. (2008) interpreted only the eastern half of the profile showing that the Precambrian crystalline basement and a thick Paleozoic-Triassic sedimentary sequence underlie the Mesozoic-Cenozoic Apulia and Apennine carbonates. Di Luzio et al. (2009) combined wide-angle refraction profiles, Bouguer gravity anomalies, receiver functions, and interpreted seismic reflection data to determine the Moho depth along the entire CROP-11. They proposed that the point of intersection between the Tyrrhenian and Adriatic plates at Moho depth (hereinafter called ITAM) could have two possible positions beneath the central Apennines. They also identified five major crustal layers, namely the Apulia carbonates, the Apennine carbonates, the upper and lower parts of the Paleozoic-Triassic sequence, and the Adriatic lower crust. Also, they suggested the presence of a detachment between the upper and lower parts of the Paleozoic-Triassic sequence. Below the crust, the Tyrrhenian side presents a hot asthenosphere related to the oceanic thinning, whereas the Adriatic side exhibits a seismic lid (e.g., Doglioni et al., 2007).

After combining the various sources of geological information summarized above, we devised a 200-km long and 40-km-thick model section with a simplified stratigraphy initially composed of seven layers (Figure 2). From top to bottom, they are as follows. S1 and S2 represent the upper crust corresponding to Apennine and Adriatic (Apulian Platform) Meso-Cenozoic carbonates and terrigenous units. S3 and S4 represent the intermediate crust, corresponding to the Paleozoic-Triassic sedimentary sequence and the crystalline basement. Notice that S4 is composed of two different bodies, with the same parameters, separated along the Tyrrhenian-Adriatic dipping boundary. S5, S6, and S7 represent the Tyrrhenian asthenospheric wedge, the lower crustal of the Adriatic slab, and the lid, respectively. The ITAM is approximately located under the Fucino basin and can take several alternative positions. The model geometry also includes a few major discontinuities representing active and potentially seismogenic faults for which the slip rate distribution will be calculated and horizontal to gently dipping detachments (see Table 1 for details). On the basis of the total geological offset, there are five normal faults (F1-5) and two thrust faults (F6-7). The two detachments are located between the asthenosphere and crust (DET) and between the lower and upper crust (DAT).

2.2.2 Model preprocessing

The preprocessing consists in building the model mesh, taking into account the discontinuities, and establishing the material parameters as well as the boundary conditions. The 2D mesh covers the entire geological section (Figure 5) with 7492 four-node quadrilateral elements and 7711 nodes. The shape, number, and size of the mesh elements vary according to the model stratigraphy and discontinuities (faults and detachments). More specifically, the mesh element size is ~0.5 km^2 near the fault planes, ~1 km^2 at the free surface, and reaches a maximum area of ~2 km^2 toward the model edges.

The boundary conditions include the gravity force and basal shear tractions. They have been applied in two load cases. The first one includes gravity only. The force is applied gradually, and the model is stabilized under the gravity. The second load case includes gravity and the basal shear tractions oriented toward the right-hand side. The gravity is inherited by the first load case, and the model is thus pre-stressed at the beginning of the second load case, where the basal tractions are activated gradually. The gradual activation of the boundary conditions over a few iterations improves the stability of the model without introducing fictitious oscillations within the model. The improvement is significant in the early evolution of the model and less apparent later. As in Hetland and Hager (2006), our model reaches a mature state but in a shorter time. The basal shear tractions represent the mantle convection in the Tyrrhenian asthenosphere and the Adriatic slab rollback. These conditions are necessary to explain the present-day contraction-extension pair across the Apennines (e.g., Doglioni et al., 1991; Doglioni et al., 1999; Rosenbaum and Lister, 2004; Doglioni et al., 2007; Barba et al., 2008, Carafa and Bird, 2016). Both conditions are simulated by north-eastward basal tractions and velocities, represented by horizontal vectors at the base of the model (Figure 5). The model bottom edge is thus allowed to move freely in the horizontal direction and is locked in the vertical direction while both sides are locked along the horizontal direction and free along the vertical direction.

The length of the model and the boundary conditions were imposed by verifying that tension and compression could coexist within the section and by taking into account that the transition between tension and compression can occur in different places depending on the material resistance to deformation and the basal shear traction. The model deformation is simulated using elasto-visco-plastic rheology: elastoplasticity from 0 km to 25 km depth for the upper and intermediate crust, and viscoplasticity from 25 km to 40 km depth (Figure 2) to reproduce the behaviour of the lid, asthenosphere, and lower crust. The viscoplastic rheology is controlled by the following equation (as implemented in our finite element software)

$$\dot{\varepsilon} = A\sigma^m\varepsilon \tag{1}$$

where $\acute{\varepsilon}$ and ε are the equivalent creep strain rate and creep strain, respectively; A is a constant; σ is the stress, and m is the stress exponent (Table 2). For stress values greater than the yield stress, the layers S5 to S7 behave plastically and the model produce plastic deformation patterns at depth as in Ellis and Stockhert (2004).

The seven faults and two detachments (Table 1) were modelled by duplicating the mesh nodes on both sides of the discontinuities (Melosh and Raefsky, 1981) so that their displacement can be introduced into the continuum problem without altering its dimensionality.

2.2.3 Model optimization through interseismic deformation

The model optimization consists in thoroughly exploring the variability of all features and parameters within physically possible ranges, in comparing the model horizontal velocity at the free surface with the reference geodetic velocity, and then validating the model using a parametric analysis.

We adopted a trial-and-error approach and used the RMS deviation as a measure to ranking the performance of each model realization. The natural variability of model parameters and lack of knowledge about some model features are taken from the pertinent literature on numerical models and geophysical investigations performed in the study area. The various model realizations incorporate variations of the geometry, rheological parameters, boundary conditions, and discontinuities (faults and detachments). The variability ranges are detailed below, and values are listed in Tables 1 and 2.

As regards the model geometry, the outline and thickness for each layer were varied in a range of approximately 5 km; the ITAM was positioned at various depths between 25 and 40 km (see Figure 2). To control the effect of the boundary conditions, we varied the model length on both sides, up to a total length of 250 km, and its thickness up to 50 km. Also, to accommodate the relative motions between the surface plate velocities from GPS data and the convecting mantle, we used a range of basal shear traction varying from 1 to 10 MPa and roll-back velocity ranging from 0 to 2 mm/yr. About the discontinuities, the fault geological kinematics was used for guiding the choice of some fault parameters, but it was not imposed in the model realizations. All faults were unlocked for various widths and exploring all combinations of locked and unlocked faults. Also, for the detachments, we examined various unlocking lengths and depth positions according to the geometry of relevant model layers (rightmost column of Table 1). We also varied the rheological parameters as described in Table 2. Mainly, we adopted low viscosity values for the asthenosphere (Tyrrhenian side) and high viscosity values for the lid and lower crust (Adriatic side).

An exhaustive exploration of all parameter ranges described above through reasonably small discrete steps would require a massive number of over 10 million possible combinations. However, not all combinations would necessarily be mutually exclusive, and a few preliminary tests revealed that many of them would produce very high RMS deviations. We thus performed approximately 3,000 model realizations and chose the realization that yielded the least RMS deviation as the best candidate model. We then validated this model choice by performing a parametric analysis of all model parameters, and verified if a small parameter alteration increases the RMS deviation significantly with respect to the best candidate model. Since the reference geodetic velocity represents the interseismic period, the best candidate model was then adopted as the best interseismic reference model.

2.3 Slip rate determination

The slip rate distribution at depth is obtained by using the best interseismic reference model while letting the faults slip to simulate the long-term behaviour. Similarly to Barba et al. (2013) and Finocchio et al. (2013), we adopted a simplified formulation and applied zero friction to the fault interface. Although usually small, the friction is never zero on a fault plane. Nonetheless, friction mostly controls the early stages of fault development, and the behaviour of hosting rocks in the near-fault region as evident from thickened layers, kinks, and drag folds in geological sections. In our case, the faults are all mature geological structures (generally formed in post-Miocene time but deemed to be still active in the Late Pleistocene - Holocene). In addition, the term of comparison for their recent activity is the horizontal geodetic velocity from very sparse GPS stations whose average distance from one another is larger than the projection to the ground surface of fault plane-widths (cf. Figure 1 and Figure 3a). This suggests that the effects of a non-zero friction would hardly be detected by the model. In all cases, with this approximation our slip rate estimates shall represent an upper limit.

Except for the fault locking status, everything else is left unchanged. We adopt a simulation time of 10 kyr. This duration is chosen to be long enough for the slip rate determination to be compared with the order of magnitude of geologically-derived slip rates, and it is also short enough for the model properties not to incur substantial changes. For example, the width of the simulated faults does not have to increase to reproduce the fault growth through propagation. We thus assume that the model properties and driving forces remain constant for the 10-kyr-long simulation time and the system is not affected by the fault slip. For each unlocked fault node, the total slip at the end of each model realization is divided by the simulation time. However, not all faults are included in every model realization. Based on considerations of their likelihood of being both active and seismogenic (Budnitz et al., 1997, Vol. 1, §4.3; Basili et al., 2013), we included F2, F3, and F7 in all realizations and alternated the remaining others in various combinations. With these constraints, we obtained 16 different fault sets. We finally estimate the uncertainty of the slip rate depth distribution by determining the maximum deviation of the slip rate within the five models with the least RMS deviation (less than 0.1 mm/yr).

3 Results

Our main results are represented by (1) an interseismic deformation model and (2) a fault long-term slip-rate model. In 1) the simulation time equals the geodetic observation time and all parameter ranges were explored; in 2) the simulation time is 10 kyr, the parameter were those of the best interseismic model obtained in 1), and only the discontinuities vary in terms of both presence and locking.

3.1 Interseismic model

The best interseismic model, i.e., the model whose velocity distribution at the free surface best fits the reference geodetic velocity, was obtained by randomly exploring the space of model parameters and calculating the RMS deviation. Table 3 summarizes the best values for each model parameter. Parametric analysis was then used to address the robustness of the best model by verifying that the RMS deviation does not further decrease by altering the best parameter values by a given amount. The results of the parametric analysis are listed in Tables 4, 5, and 6 (based on RMS in the rightmost column) and best model values are those in Table 3 (see also Figures A1, A2, A3, and A4 in the Parametric Analysis Section of the supplementary document).

Figure 6 shows the horizontal velocity predicted by the best interseismic model compared with the geodetic filtered velocity. The modelled velocity has only small fluctuations around the reference velocity, yet always within the confidence intervals, and the most significant deviation is localized at around 150 km along the section. The overall difference is thus irrelevant and quantified by an RMS deviation of 0.07 mm/yr.

The structural architecture of the best model includes the seven layers (S1-S7) shown in Figure 2. We found in particular that S3 behaves elastically because the data are not sensitive to yield stress values larger than 0.3 GPa and the Young's modulus in S3 is higher than those in the surrounding layers. We also found that eastward-oriented forces, applied at the base of the model in the form of shear traction and velocity conditions, are necessary. Shear traction applied in correspondence with the asthenosphere and lid took the values of 6.0 MPa and 4.5 MPa, respectively. The eastward velocity applied to the slab had to be 0.55 mm/yr. All of the faults appeared to be fully locked except for F2, which has to be unlocked for its lowermost width of 10 km. Note that F2 is the fault that generated the M 6.9, Avezzano earthquake in 1915. A good fit of the velocity distribution also requires the presence of an 85-km-long detachment at the top of the asthenosphere (Table 6). Figure A5 in the Strain Plots Section of the supplementary document shows the total strain and plastic strain of the best interseismic model.

3.2 Long-term slip rate model

The slip rate was calculated for each fault in 16 possible combinations of fault existence. The average slip rate at depth for the 16 fault combinations is shown in Figure 7a and Table 7.

In particular, for each slip rate depth distribution, Table 7 lists the maximum and average values. To better appreciate the depth distribution Table 7 also show an asymmetry ratio f given by

$$f = \frac{Z_x - Z_t}{Z_b - Z_t} \quad (2)$$

where Z_x is the depth of the maximum slip rate value on the fault, and Z_t and Z_b are the depths of the top and bottom edge of the fault, respectively. The ratio f tends to 0 when the maximum slip rate is near the top edge, tends to 1 when the maximum slip rate is near the bottom edge, and tends to be equal or close to 0.5 when the maximum slip rate is the middle of the fault.

F3, F5, and F6 show f-values in the range 0.6-1.0, meaning that the maximum slip rate is systematically located in the lower third of the fault. F7 has the maximum slip rate confined in the upper half except for the SR13 combination (f=0.7). In F1, F2, and F4 the maximum slip rate is mostly located near the top of the fault.

Depending on which fault configuration is chosen, the slip rate can be significantly different for each different fault. The range of slip rate depth average for each fault varies up to a maximum of ~2.5 mm/yr with an overall average slip rate of approximately 1.1 mm/yr for normal faults and 0.2 mm/yr for thrust faults.

Recalling that the fault kinematics is not imposed in the model, we found that most of the faults maintain the same sense of movement in any of the 16 combinations, except for F4 and F7 that behave like a normal or reverse fault depending on which fault combination they are included in. In particular, F4 acts as a thrust fault only when it is in the same fault combination with F5. Despite having a total geological offset of reverse type, F6 works in all combinations like a normal fault. In a few combinations, F4 and F7 also show an inverted sense of movement with respect to their total geological offset. The implications of these results will be discussed later, while the results for all 16 combinations are listed in Table A1 in the Slip Rates Section of the supplementary document.

Figure 7 show the results for SR01 (which includes F2, F3, F4, and F7) which we selected as our preferred fault combination (see Table 7 for numeric values) and Figure A6 (in the Strain Plots Section of the supplementary document) shows the total strain and plastic strain. In SR01, F4 has a rather uniform slip rate depth distribution. F2, instead, has a rather uniform slip rate distribution only in its shallower half whereas below 6 km depth the slip rate gradually decreases until it becomes one-fourth lower than the slip rate at the free surface. Conversely, the slip rate varies significantly with depth for F7 and F3. F7 has a slip rate peak at approximately 5 km depth, close to the fault top. F3 has a maximum slip rate near the bottom, at about 13-14 km depth, and the maximum slip rate at depth is three times higher than its slip rate at the free surface.

The slip rate uncertainty has small variations with depth, although the uncertainty range is not symmetric on the mean value (Figure 7b). F7 and F4 have the largest maximum uncertainty ranges, reaching approximately 0.3 mm/yr and 0.5 mm/yr, respectively. The uncertainty of the average slip rate for F2, F3, F4, and F7 is 2%, 7%, 20%, and 40%, respectively.

4 Discussion

In this work, we have explored the use of finite-element models to calculate the distribution of slip rate at seismogenic depth for several faults at once. An important aspect of our approach is that faults are let free to slip under the drive of tectonic forces regardless of their geologically-determined offset. In this way, any fault in the model is just seen as a crustal discontinuity and its behaviour only reflects the amount of slip that is necessary for the movement of the model free surface to keep the pace of the independently-measured geodetic velocity. Our case study is set in the central Apennines, Italy, where normal and reverse faults coexist at a short distance from one another. Our results are represented by 1) an interseismic deformation model that provides insights into the geological structure and fault locking; and 2) a long-term fault slip rate model that provides insights on how the slip rate is distributed at depth while the on-fault and off-fault overall deformation is partitioned among the various model features.

4.1 Interseismic model

The interseismic deformation model was chosen as the model with the best performance among several thousand trials in reproducing the reference geodetic velocity under the assumption of fault locking. The main limitation of this approach is represented by the unavailability of GPS data in the offshore part of the model. Knowing that a few tectonic indicators (e.g. major faults, earthquake focal mechanisms) suggest the presence of a compressional state of stress in this region, we assumed that the horizontal velocity tapers to zero in the Adriatic Sea (30 km outside the model section) and, therefore, the modelled horizontal velocity (Figure 6) was not constrained by the data. Therefore, potentially existing faults in the offshore region cannot be studied with this particular modelling approach. However, the model is well constrained by both geodetic and stress data in the Apennine interiors where the best interseismic model indicates that F2 is unlocked. Therefore, the model suggests that the actual strain conditions in that area are still affected by postseismic relaxation that follows the M 6.9, Avezzano earthquake of 1915. The postseismic relaxation is known to last tens of years (Pollitz et al., 2006) and the postseismic effects of the Avezzano earthquake were already revealed by the analysis of elevation changes occurred over 85 years at a distance of about 25 km from the F2 surface trace (Amoruso et al., 2005). However, even in regions where the data are of high quality, the GPS data are not sensitive to fault unlocked sections shorter than 10 kilometres. Thence, the locking width we have found in the interseismic model cannot be used in applications such as the short-term seismic hazard estimates unless additional considerations about fault behaviour are made.

The interseismic deformation model also provides insights into the geological layering and the geodynamic context of the area. The southwestern part of the section, i.e. to the southwest of all the faults, is characterized by the presence of a rigid layer (S3; Figure 2). This layer corresponds to a structural high made of Triassic dolomites (Di Luzio et al., 2009) that are also known for the seismic and magnetic properties (Chiarabba et al., 2010; Speranza and Minelli, 2014). Our model confirms the presence of this layer because either decreasing its rigidity or increasing its plasticity causes a significant lack of fit with the reference geodetic velocity. We also found a better fit (smaller RMS deviation) when a thinner Tyrrhenian crust is used, and the ITAM is located in a position more similar to that proposed by Doglioni et al. (1991) or Di Stefano et al. (2009) and closer to the westernmost position of those suggested by Di Luzio et al. (2009). From the geodynamic viewpoint, the model indicates that an asthenospheric shear on the Tyrrhenian side and a slab rollback on the Adriatic side are required, in agreement with Barba et al. (2008, and references therein) to significantly minimizing the RMS deviation. These boundary conditions thus affect the state of stress and strain within the crust and, together with the other structural and kinematic features control the transition from the extensional to the contractional domain, and ultimately determine the fault kinematics.

4.2 Long-term slip rate model

Estimating the behaviour of faults on a longer term than that of the interseismic period is not only useful for improving our understanding of the geodynamic and paleoseismic history of an area, but also for practical applications, such as the seismic hazard assessment, especially if performed with a probabilistic approach. The time simulated by the long-term slip-rate model, 10 kyr, is much longer than the GPS observation time. Therefore, this model setup neither simulate variations in the state of stress or model driving forces nor predict processes that occur on a time scale of 10^5-10^6 years, such as fault growth and propagation, or the waning or waxing of fault activity. In our model, however, the fault slip is determined as a consequence of off-fault strain, and this implies that improving the knowledge of rock rheological properties or subsurface stratigraphy will improve accuracy and robustness of the model slip rate. Our method, therefore, represents an independent and complementary strategy with respect to geologic slip rate estimates that depend upon the quality and number of on-fault field observations (e.g., Pantosti et al., 1996) or to numerical estimates from retrodeformed geological sections, which depend on the quality of geophysical data and are usually representative of long time intervals (e.g., Maesano et al., 2013). As such, our method is also a tool to compensate the possible deficit of geologic knowledge on specific active faults. Since vertical 2D models can easily include gravity, stratification, and traction, our modelling approach is also complementary to horizontal 2D models that provide the slip rate distribution along the fault trace (e.g., Bird, 2009; Cowie et al., 2012).

The 2D approach, however, has inherent limitations, one of which is the possible out-of-plane motion, i.e. motion in the direction perpendicular to the model section. On the one hand, this problem can be solved by 3D models and their use represents a necessary course of action for future work. On the other hand, in the particular case of our model, the 2D section is not only parallel to the main stress direction, but it is also perpendicular to the strike of main faults. Therefore, our slip rate estimates represent well the dip-slip component of the slip rate. We also notice that earthquake focal mechanisms in this region (Figure 3a) have a very small strike-slip component. We are thus confident that while the overall interseismic out-of-plane motion is certainly significant as also shown by the normal-to-section component of the GPS horizontal velocity (Figure 3a), the strike-slip component of slip rate should be limited if not negligible.

The slip rate values obtained from our models are rather different from those available in the literature and obtained through various approaches (Figure 7). Having adopted the zero-friction assumption one would expect our slip rate to systematically overestimate, though by small amount, the geological slip rate. We found a rather different situation, described below, which requires a case-by-case explanation of the possible reasons of the discrepancies.

With regard to normal faults (F1-5), our slip rate values are generally higher than those so far proposed by interpreting on-fault shallow geological data. Apart from a few exceptions, most normal fault slip rates based on geological point data rarely exceed 1 mm/yr (Galadini and Galli, 2000; Papanikolaou et al., 2005; Pace et al., 2006; Akinci et al., 2009). Indeed, our model shows that only F3 has average slip rate values smaller than 1 mm/yr in all fault combinations except one. F1 and F4 are slower than 1 mm/yr only in a few fault combinations, with F4 sometimes showing an inverted sense of movement with respect to the total geological offset. F2 and F5 are always faster than 1 mm/yr. The two fault combinations that include all five normal faults (SR12 and SR16) require that F5 has an inverted sense of movement. In our preferred fault combination, only F3 has a mean slip rate lower than 1 mm/yr. We tentatively explain these systematic results in either of two ways on the basis of how most on-fault slip rates for normal faults in the central Apennines are estimated: 1) they are based on very shallow-depth (few metres for paleoseismic data) or ground-surface displacement that only capture a portion of the total slip rate and thus represent a lower limit; 2) they are derived from point data acquired on closely spaced, sub-parallel fault strands that may represent splays of the same master fault at depth. Conversely, with regard to thrust faults (F6-7), our slip rate values are systematically lower than those proposed by interpreting subsurface data. In particular, F6 seems to have reversed its sense of movement. The thrust faults incorporated in our models are actually those located just to the east of the extension-contraction transition and at the southern end of the central Apennines fold-and-thrust wedge, whereas most of the thrust faults for which the slip rates were previously estimated are located in a more central and external position of the central Apennines fold-and-thrust wedge, on the Adriatic coast or offshore. In addition, most of these thrust-fault slip rates refer to geological markers that span a much longer time window (~0.1-5.0 My; Vannoli et al., 2004; Bigi et al., 2013; Maesano et al., 2013) than that of our model. We can explain this slip rate discrepancy with the help of our preferred fault combination. F6 can be currently (last 10 kyr) involved in the extensional domain and F7 can be experiencing a phase of relative quiescence with respect to a faster, longer-term average rate. Alternatively, as sometimes observed for other faults of the fold-and-thrust wedge (Maesano and D'Ambrogi 2015; Maesano et al., 2015), F7 could be in its late waning stage before deactivation, considering that the inception age of F7 is rather old (likely Messinian) and thrust faults in the central Apennines have an average lifespan of approximately 5 My (Basili and Barba, 2007).

4.3 Uncertainties and seismic hazard implications

The uncertainty of model parameters could not be formally propagated throughout the simulation procedure onto the slip rate estimates because not all sources of uncertainties and their amount were known and the formal propagation of errors of uncertain origin could have become deceptive. As a safe measure, we have then chosen to adopt the variability arising from model realizations with RMS deviation smaller than 0.1 mm/yr as the possible variability affecting our fault slip rate estimates. This choice corresponds to five models (Table 4, models EP04, EP07, EP09, EP11, and EP26) with equally significant slip rates. Such slip rate estimates (see Figure 7) thus incorporate a quantification of the epistemic uncertainty related to the level of knowledge of faults that is of primary interest, especially in seismic hazard applications. However, to address which fault set is more reliable than others requires that additional research and a critical review of the data be carried out on these faults. The choice of the fault set is beyond the scope of this work, and we have thus provided the information on the model slip rates for all fault sets in the Slip Rates Section of the supplementary document.

Knowledge of slip rate at depth is important because its variations affect earthquake depth distributions (Nadeau et al., 1999). We have shown that the slip rate at seismogenic depth, as predicted by physically plausible modelling, can take different shapes even when the faults are close to each other and presumably controlled by similar tectonic conditions. This consideration implies that also the earthquake depth distribution may vary significantly for faults located at short distance from one another. Additional implications can then be devised if slip rate depth distributions, as opposed to slip rate depth averages, are used to derive the earthquake rates in applications such as probabilistic seismic hazard analysis. Assuming that the cumulative long-term slip rate results from the sum of an unspecified number of fault slip events, the probability of future fault slip events is higher where slip rate is higher and vice versa. Therefore, provided that slip rates are properly used to equate tectonic/geodetic moment rates to seismic moment rates, the slip rate variation with depth and its uncertainties could severely affect the predicted ground shaking because of the consequent upward or downward shift of earthquake occurrences. In our preferred fault combination, for example, F2 would likely be relatively more earthquake-productive than F3 at a shallow depth and thus be more hazardous than expected from using its depth-averaged slip rate. These considerations, however, will strongly depend on the strategy adopted in estimating the ground shaking. For example, the use of a ground-motion prediction equation that uses the Joyner-Boore fault-to-site distance metric would be totally ineffective in reflecting the slip rate depth distribution for the near-fault shaking.

5 Conclusions

We modelled the crustal deformation that fits the geodetic surface horizontal velocity along a SW-NE profile in central Italy by taking into account: 1) westward-directed shear basal traction, 2) slab roll-back, 3) presence of a detachment in the Tyrrhenian side, 3) presence of seven major crustal faults (F1-7). Our main results are represented by an interseismic model and a long-term slip-rate model.

In the interseismic stage, although the majority of the faults appear to be fully locked, F2 (i.e. the fault that generated the Avezzano, M 6.9 earthquake in 1915) appears to be mostly unlocked. This observation is consistent with the higher gradient of GPS velocities across this fault zone and could represent a late stage of the fault post-seismic activity. The average long-term slip rate at depth is approximately 1.1 mm/yr for normal faults and 0.2 mm/yr for thrust faults. Concerning previous slip rate estimates, most of which derive from the interpretation of surface or very shallow geologic data, our slip rate values are systematically higher for normal faults and lower for thrust faults. Of all investigated faults, F6 has a peculiar behaviour. It is located at the transition between the extensional and contractional domains, and its present-day kinematics remains unclear. In all of our model trials, F6 behaves as a normal fault despite being known to have a total geologic offset of reverse type. This implies that this fault should have changed its sense of movement in the last 10 kyr. In other words, the NE migration of the extension-contraction pair could have reached the F6 location in geologically recent times.

We maintain that our slip-rate results is a viable representation of the tectonic activity of these faults at seismogenic depth and that they may exceed the values obtained by observations limited to the shallowest portion of the crust which is affected by near-surface processes. The reasons why these discrepancies exist should be the matter of future investigations. Our model slip rates also take different shapes at depth even where the faults are close to each other. This fact is visible in most of the fault combinations used in our slip-rate calculations. We thus suggest that the presence of similar or apparently similar tectonic characteristics across several faults is not a sufficient condition to generate similar distributions of slip rate at depth. Therefore, the extrapolation at depth of slip-rates that reflect the surface activity of faults - a commonly adopted strategy in tectonic studies - should be used with more caution.

For preparing the way to incorporate our results into probabilistic seismic hazard assessment, we considered both epistemic and aleatory uncertainties of model parameters. These uncertainties should be thoughtfully combined with the uncertainties related to the seismic hazard calculations to avoid their over or under representation and to evaluate the mutual interdependency with other sources of uncertainties. However, we underline that the uncertainties arising from our model are of the same order of magnitude of, if not smaller than, the uncertainties associated with classical geological models. Also, the construction of our model adopts a reproducible procedure that will allow the reduction of uncertainties whenever further information or data become available.

Acknowledgments

The work was supported by Project "Abruzzo" (code: RBAP10ZC8K_003) funded by the Italian Ministry of Education, University and Research (MIUR), which is gratefully acknowledged. We thank M. M. C. Carafa for reviewing an early version of the manuscript. We also thank S. Ellis and J. J. Martínez-Díaz for their insightful reviews and suggestions that substantially improved the paper.

Tables

Table 1 – Summary of literature data on modelled active faults and parameters used for modelling.

Fault Code	Fault Name	Dip	Depth range*	References	Model depth*	Model dip	Model unlocked width[§]
		deg	km		km	deg	km
F1	Val Roveto	c. 50	c. 0-15	1	1-15	50	0-15
F2	Avezzano	50	1-15	2	1-15	50	0-15
F3	Aquila-Borbona	50	2-14	2	1-15	50	0-15
F4	Sulmona	50	1-14	2	1-15	50	0-15
F5	Caramanico	c. 50	c. 0-15	3	1-15	50	0-15
F6	Citeriore Deep	30	8-18	2	8-17	30	0-9
F7	Citeriore Shallow	30	3-8	2	3-15	30	0-12
DET	Apennine detachment	Horizontal	-	4,5	-	Horizontal	0-90
DAT	Adriatic detachment	Horizontal	-	5	-	Horizontal	0-30

*top-bottom; [§]minimum-maximum. References: (1) Tozer et al. (2002); (2) DISS Working Group (2015); (3) Ghisetti and Vezzani (2002); (4) Doglioni et al. (1991); (5) Di Luzio et al. (2009).

Table 2 - Ranges of tested parameters (minimum-maximum values) used in numerical model computations.

Layer Code	Layer Name	Density (1,2,4,5)	Young modulus (3,4,5)	Yield stress (3,4,5)	Poisson ratio (3,4,5)	A* (6)	m* (6)
		kg/m^3	GPa	GPa		$Pa^{-m}\ s^{-1}$	
S1	Upper Crust	2.2-2.7	1-50	0.1-0.4	0.1-0.4	-	
S2	Upper Crust	2.2-2.7	1-50	0.1-0.5	0.1-0.4	-	
S3	Intermediate Crust	2.5-3.0	10-120	0.1-0.5	0.1-0.4	-	
S4	Intermediate Crust	2.5-3.0	10-100	0.1-0.5	0.1-0.4	-	
S5	Asthenosphere	3.2-3.5	20-200	0.1-0.7	0.1-0.4	$5x10^{-18} – 5x10^{-95}$	8-13
S6	Lower Crust	3-3.5	20-80	0.1-0.7	0.1-0.4	$5x10^{-18} – 5x10^{-95}$	8-13
S7	LID	3.3-3.5[1,2]	20-200	0.1-0.7	0.1-0.4	$5x10^{-18} – 5x10^{-95}$	8-13

* Terms in Eq. (1). References: (1) Di Luzio et al., 2009; (2) Tiberti et al., 2005; (3) Tizzani et al., 2013; (4) Megna et al., 2008; (5) Finocchio et al., 2013; (6) Supplementary Material in Barba et al., 2013.

Table 3 - Best-fitting model parameters: (top) layer material properties; (bottom) boundary conditions and faults.

Layer Code	Layer Name	Density	Young modulus	Yield stress	Poisson ratio	A*	m*
		kg/m^3	GPa	GPa		$Pa^{-m} s^{-1}$	
S1	Upper Crust	2.5	8	0.24	0.25	-	
S2	Upper Crust	2.5	9	0.27	0.25	-	
S3	Intermediate Crust	2.7	50	0.3	0.25	-	
S4	Intermediate Crust	2.7	40	0.2	0.25	-	
S5	Asthenosphere	3.3	100	0.3	0.25	$5x10^{-40}$	12
S6	Lower Crust	3.3	50	0.3	0.25	$5x10^{-90}$	12
S7	LID	3.3	100	0.3	0.25	$5x10^{-90}$	12

* Terms in Eq. (1).

Bound. cond. or fault	Unlocked width	Shear traction	Velocity
	km	MPa	mm/yr
F2	10	-	-
DET	85	-	-
F1,F3-F7,DAT	0	-	-
Asthenosphere	-	6	-
LID	-	4.5	-
Slab	-	-	0.55

Table 4 – Results of the parametric analysis for elastic parameters with RMS deviations.

Model Code	Layer Code	Young modulus	Yield stress	RMS
		GPa	GPa	mm/yr
EP01	S1	1	0.24*	0.20
EP02	S1	30	0.24*	0.31
EP03	S1	8*	0.1	0.18
EP04	S1	8*	0.3	0.08
EP05	S2	1	0.27*	0.56
EP06	S2	30	0.27*	0.12
EP07	S2	9*	0.4	0.08
EP08	S2	9*	0.1	0.31
EP09	S3	100	0.3*	0.09
EP10	S3	10	0.3*	0.34
EP11	S3	50*	0.4	0.07
EP12	S3	50*	0.1	0.80
EP13	S4	60	0.2*	0.11
EP14	S4	20	0.2*	0.10
EP15	S4	40*	0.1	0.16
EP16	S4	40*	0.4	0.15
EP17	S5	130	0.3*	0.10
EP18	S5	50	0.3*	0.18
EP19	S5	100*	0.6	0.33
EP20	S5	100*	0.1	0.44
EP21	S6	20	0.3*	0.45
EP22	S6	80	0.3*	0.15
EP23	S6	50*	0.5	0.34
EP24	S6	50*	0.2	0.23
EP25	S7	50	0.3*	0.12
EP26	S7	130	0.3*	0.09
EP27	S7	100*	0.1	0.17
EP28	S7	100*	0.5	0.10

* individual best-model value (Table 3).

Table 5 - Results of the parametric analysis for boundary conditions with RMS deviations.

Model Code	Varied boundary condition	Shear AST	Shear LID	ITAM depth	Slab Displ.	RMS
		MPa	MPa	Km	mm/yr	mm/yr
BC01	ITAM depth	6*	4.5*	35	0.55*	0.12
BC02	ITAM depth	6*	4.5*	40	0.55*	0.16
BC03	Shear AST	0	4.5*	30*	0.55*	0.20
BC04	Shear AST	4	4.5*	30*	0.55*	0.10
BC05	Shear AST	10	4.5*	30*	0.55*	0.14
BC06	Shear LID	6*	0	30*	0.55*	0.16
BC07	Shear LID	6*	10	30*	0.55*	0.21
BC08	Slab Displ.	6*	4.5*	30*	0	1.28
BC09	Slab Displ.	6*	4.5*	30*	1	1.39

* individual best-model value (Table 3).

Table 6 - Results of the parametric analysis for unlocked faults and detachments with RMS deviations; all other parameters are those of the best model (Table 3).

Model Code	Unlocked-fault Code	Unlocked width	RMS
		km	mm/yr
UL01	All locked	-	0.11
UL02	F1	10	0.24
UL03	F3	10	0.11
UL04	F4	10	0.12
UL05	F5	10	0.17
UL06	F6	10	0.35
UL07	F7	10	0.10
UL08	DET	15	0.90
UL09	DAT	15	0.10
UL10	All unlocked	10	0.27

Table 7 - Modelled slip rates (average/maximum; in mm/yr) and parameter *f* for the seven faults (F1-F7) in the 16 combinations (SR01-SR16).

	F1			F2			F3			F4			F5			F6			F7		
	avg	*max*	*f*	*avg*	*max*	*f*	*avg*	*max*	*f*	*Avg*	*max*	*f*	*avg*	*max*	*f*	*avg*	*Max*	*f*	*avg*	*max*	*f*
SR01*	-	-	-	-1.89	-2.05	0.29	-0.64	-0.98	0.92	-1.24	-1.31	0.00	-	-	-	-	-	-	0.10	0.15	0.22
SR02	-	-	-	-1.72	-2.10	0.00	-0.56	-1.00	0.92	-	-	-	-2.38	-2.52	0.87	-	-	-	0.20	0.27	0.30
SR03	-1.94	-2.32	0.00	-1.33	-1.39	0.49	-0.90	-1.02	0.82	-	-	-	-	-	-	-	-	-	0.14	0.21	0.26
SR04	-	-	-	-2.00	-2.13	0.29	-1.43	-1.64	0.85	-	-	-	-	-	-	-	-	-	0.07	0.12	0.17
SR05	-	-	-	-1.74	-1.98	0.00	-0.97	-1.18	0.85	-	-	-	-	-	-	-0.93	-1.31	0.90	-0.15	-0.20	0.48
SR06	-1.36	-1.76	0.00	-1.34	-1.48	0.18	-0.74	-0.95	0.85	-	-	-	-	-	-	-0.74	-1.06	0.90	-0.07	-0.10	0.50
SR07	-1.51	-1.99	0.00	-1.40	-1.50	0.47	-0.55	-0.82	0.92	-0.87	-0.92	0.00	-	-	-	-	-	-	0.13	0.19	0.24
SR08	-1.03	-1.48	0.00	-1.42	-1.71	0.00	-0.42	-0.76	0.90	-	-	-	-2.05	-2.18	0.85	-	-	-	0.20	0.28	0.30
SR09	-	-	-	-1.73	-2.13	0.00	-0.58	-1.00	0.90	-0.22	-0.38	0.03	-2.45	-2.55	0.82	-	-	-	0.19	0.26	0.30
SR10	-	-	-	-1.70	-1.96	0.00	-0.62	-0.91	0.90	-0.62	-0.64	0.21	-	-	-	-0.83	-1.18	0.90	-0.12	-0.16	0.52
SR11	-	-	-	-1.66	-2.03	0.00	-0.54	-0.94	0.90	-	-	-	-2.03	-2.11	0.77	-0.36	-0.56	0.90	0.10	0.14	0.24
SR12	-0.97	-1.44	0.00	-1.45	-1.76	0.00	-0.44	-0.84	0.92	-0.22	-0.36	0.03	-2.19	-2.29	0.85	-	-	-	0.20	0.27	0.30
SR13	-1.21	-1.64	0.00	-1.35	-1.52	0.18	-0.52	-0.75	0.90	-0.46	-0.47	0.21	-	-	-	-0.70	-1.00	0.88	-0.06	-0.08	0.70
SR14	-0.92	-1.37	0.00	-1.40	-1.69	0.00	-0.41	-0.78	0.90	-	-	-	-1.83	-1.91	0.77	-0.33	-0.51	0.90	0.12	0.16	0.24
SR15	-	-	-	-1.66	-2.05	0.00	-0.57	-0.92	0.90	-0.16	-0.38	0.00	-2.07	-2.11	0.67	-0.38	-0.58	0.90	0.08	0.12	0.22
SR16	-0.89	-1.35	0.00	-1.42	-1.71	0.00	-0.43	-0.79	0.90	-0.15	-0.35	0.00	-1.87	-1.92	0.69	-0.34	-0.53	0.90	0.10	0.14	0.22

* preferred combination.

References

Akinci, A., Galadini, F., Pantosti, D., Petersen, M., Malagnini, L., Perkins, D., 2009. Effect of Time Dependence on Probabilistic Seismic-Hazard Maps and Deaggregation for the Central Apennines, Italy. Bulletin of the Seismological Society of America 99, 585-610, doi: 10.1785/0120080053.

Albano, M., Barba, S., Saroli, M., Moro, M., Malvarosa, F., Costantini, M., Bignami, C., Stramondo, S., 2015. Gravity-driven postseismic deformation following the Mw 6.3 2009 L'Aquila (Italy) earthquake. Sci Rep 5, 16558, doi: 10.1038/srep16558.

Allmendinger, R.W., 1998. Inverse and forward numerical modeling of trishear fault-propagation folds. Tectonics 17, 640-656, doi: 10.1029/98tc01907.

Amoruso, A., Crescentini, L., D'Anastasio, E., De Martini, P.M., 2005. Clues of postseismic relaxation for the 1915 Fucino earthquake (central Italy) from modeling of leveling data. Geophysical Research Letters 32, doi: 10.1029/2005gl024139.

Barba, S., Basili, R., 2000. Analysis of seismological and geological observations for moderate size earthquakes: the Colfiorito Fault System (Central Apennines, Italy). Geophysical Journal International 141, 241-252, doi.

Barba, S., Carafa, M.M.C., Boschi, E., 2008. Experimental evidence for mantle drag in the Mediterranean. Geophysical Research Letters 35, doi: 10.1029/2008gl033281.

Barba, S., Finocchio, D., Sikdar, E., Burrato, P., 2013. Modelling the interseismic deformation of a thrust system: seismogenic potential of the Southern Alps. Terra Nova 25, 221-227, doi: 10.1111/ter.12026.

Basili, R., Barba, S., 2007. Migration and shortening rates in the northern Apennines, Italy: implications for seismic hazard. Terra Nova 19, 462-468, doi: 10.1111/j.1365-3121.2007.00772.x.

Basili, R., Tiberti, M.M., Kastelic, V., Romano, F., Piatanesi, A., Selva, J., Lorito, S., 2013. Integrating geologic fault data into tsunami hazard studies. Natural Hazards and Earth System Science 13, 1025-1050, doi: 10.5194/nhess-13-1025-2013.

Benedetti, L., Manighetti, I., Gaudemer, Y., Finkel, R., Malavieille, J., Pou, K., Arnold, M., Aumaître, G., Bourlès, D., Keddadouche, K., 2013. Earthquake synchrony and clustering on Fucino faults (Central Italy) as revealed from in situ36Cl exposure dating. Journal of Geophysical Research: Solid Earth 118, 4948-4974, doi: 10.1002/jgrb.50299.

Bigi, S., Conti, A., Casero, P., Ruggiero, L., Recanati, R., Lipparini, L., 2013. Geological model of the central Periadriatic basin (Apennines, Italy). Marine and Petroleum Geology 42, 107-121, doi: 10.1016/j.marpetgeo.2012.07.005.

Bird, P., 1989. New finite element techniques for modeling deformation histories of continents with stratified temperature-dependent rheologies. Journal of Geophysical Research 94, 3967-3990, doi.

Bird, P., 1999. Thin-plate and thin-shell finite-element programs for forward dynamic modeling of plate deformation and faulting. Computers & Geosciences 25, 383-394, doi.

Bird, P., 2009. Long-term fault slip rates, distributed deformation rates, and forecast of seismicity in the western United States from joint fitting of community geologic, geodetic, and stress direction data sets. Journal of Geophysical Research 114, doi: 10.1029/2009jb006317.

Bonini, L., Basili, R., Toscani, G., Burrato, P., Seno, S., Valensise, G., 2015. The role of pre-existing discontinuities in the development of extensional faults: An analog modeling perspective. Journal of Structural Geology 74, 145-158, doi: 10.1016/j.jsg.2015.03.004.

Bonini, L., Di Bucci, D., Toscani, G., Seno, S., Valensise, G., 2014. On the complexity of surface ruptures during normal faulting earthquakes: excerpts from the 6 April 2009 L'Aquila (central Italy) earthquake (Mw 6.3). Solid Earth 5, 389-408, doi: 10.5194/se-5-389-2014.

Bray, J.D., Seed, R.B., Cluff, L.S., Seed, H.B., 1994. Earthquake fault propagation through soil. Journal of Geotechnical Engineering 120, 543-561, doi: 10.1061/(ASCE)0733-9410(1994)120:3(543).

Budnitz, R.J., Apostolakis, G., Boore, D.M., Cluff, L.S., Coppersmith, K.J., Cornell, C.A., Morris, P.A., 1997. Recommendations for probabilistic seismic hazard analysis: guidance on uncertainty and the use of experts. US Nuclear Regulatory Commission, NUREG/CR-6372, Washington, D.C.

Carafa, M.M.C., Barba, S., 2011. Determining rheology from deformation data: The case of central Italy. Tectonics 30, n/a-n/a, doi: 10.1029/2010tc002680.

Carafa, M.M.C., Barba, S., 2013. The stress field in Europe: optimal orientations with confidence limits. Geophysical Journal International 193, 531-548, doi: 10.1093/gji/ggt024.

Carafa, M.M.C., Barba, S., Bird, P., 2015. Neotectonics and long-term seismicity in Europe and the Mediterranean region. Journal of Geophysical Research: Solid Earth 120, 5311-5342, doi: 10.1002/2014jb011751.

Carafa, M.M.C., Bird, P., 2016. Improving deformation models by discounting transient signals in geodetic data, II: Geodetic data, stress directions, and long-term strain rates in Italy. Journal of Geophysical Research: Solid Earth, n/a-n/a, doi: 10.1002/2016JB013038.

Chamlagain, D., Hayashi, D., 2005. Fault development in the Thakkhola half graben: insights from numerical simulation. Bulletin of the Faculty of Science, University of the Ryukyus, Japan. 79, 57-90, doi.

Chiarabba, C., Amato, A., Anselmi, M., Baccheschi, P., Bianchi, I., Cattaneo, M., Cecere, G., Chiaraluce, L., Ciaccio, M.G., De Gori, P., De Luca, G., Di Bona, M., Di Stefano, R., Faenza, L., Govoni, A., Improta, L., Lucente, F.P., Marchetti, A., Margheriti, L., Mele, F., Michelini, A., Monachesi, G., Moretti, M., Pastori, M., Piana Agostinetti, N., Piccinini, D., Roselli, P., Seccia, D., Valoroso, L., 2009. The 2009 L'Aquila (central Italy) MW6.3 earthquake: Main shock and aftershocks. Geophysical Research Letters 36, doi: 10.1029/2009gl039627.

Chiarabba, C., Bagh, S., Bianchi, I., De Gori, P., Barchi, M., 2010. Deep structural heterogeneities and the tectonic evolution of the Abruzzi region (Central Apennines, Italy) revealed by microseismicity, seismic tomography, and teleseismic receiver functions. Earth and Planetary Science Letters 295, 462-476, doi: 10.1016/j.epsl.2010.04.028.

Chiaraluce, L., 2003. Imaging the complexity of an active normal fault system: The 1997 Colfiorito (central Italy) case study. Journal of Geophysical Research 108, doi: 10.1029/2002jb002166.

Cowie, P.A., Roberts, G.P., Bull, J.M., Visini, F., 2012. Relationships between fault geometry, slip rate variability and earthquake recurrence in extensional settings. Geophysical Journal International 189, 143-160, doi: 10.1111/j.1365-246X.2012.05378.x.

Cowie, P.A., Vanneste, C., Sornette, D., 1993. Statistical physics model for the spatiotemporal evolution of faults. Journal of Geophysical Research 98, 21809, doi: 10.1029/93jb02223.

Devoti, R., Esposito, A., Pietrantonio, G., Pisani, A.R., Riguzzi, F., 2011. Evidence of large scale deformation patterns from GPS data in the Italian subduction boundary. Earth and Planetary Science Letters 311, 230-241, doi: 10.1016/j.epsl.2011.09.034.

Di Luzio, E., Mele, G., Tiberti, M.M., Cavinato, G.P., Parotto, M., 2009. Moho deepening and shallow upper crustal delamination beneath the central Apennines. Earth and Planetary Science Letters 280, 1-12, doi: 10.1016/j.epsl.2008.09.018.

Di Stefano, R., Kissling, E., Chiarabba, C., Amato, A., Giardini, D., 2009. Shallow subduction beneath Italy: Three-dimensional images of the Adriatic-European-Tyrrhenian lithosphere system based on high-qualityPwave arrival times. Journal of Geophysical Research 114, doi: 10.1029/2008jb005641.

DISS, W.G., 2015. Database of Individual Seismogenic Sources (DISS), Version 3.2.0: A compilation of potential sources for earthquakes larger than M 5.5 in Italy and surrounding areas. Istituto Nazionale di Geofisica e Vulcanologia, http://diss.rm.ingv.it/diss/, doi: 10.6092/INGV.IT-DISS3.2.0.

Doglioni, C., Carminati, E., Cuffaro, M., Scrocca, D., 2007. Subduction kinematics and dynamic constraints. Earth-Science Reviews 83, 125-175, doi: 10.1016/j.earscirev.2007.04.001.

Doglioni, C., Gueguen, E., Harabaglia, P., Mongelli, F., 1999. On the origin of W-directed subduction zones and applications to the western Mediterranean. Geological Society, London Special Publication 156, 541-561, doi.

Doglioni, C., Moretti, I., Roure, F., 1991. Basal lithospheric detachment, eastward mantle flow and Mediterranean Geodynamics: a discussion. Journal of Geodynamics 13, 47-65, doi.

Ellis, S., Stöckhert, B., 2004. Imposed strain localization in the lower crust on seismic timescales. Earth Planets Space 56, 1103-1109, doi.

Elter, P., Giglia, G., Tongiorgi, M., Trevisan, L., 1975. Tensional and compressional areas in the recent (Tortonian to Present) evolution of the northern Apennines. Bollettino di Geofisica Teorica ed Applicata 65, 3-18, doi.

Fantoni, R., Franciosi, R., 2010. Tectono-sedimentary setting of the Po Plain and Adriatic foreland. Rendiconti Lincei 21, 197-209, doi: 10.1007/s12210-010-0102-4.

Finocchio, D., Barba, S., Santini, S., Megna, A., 2013. Interpreting the interseismic deformation of the Altotiberina Fault (central Italy) through 2D modelling. Annals of Geophysics 56, S0673, doi: 10.4401/ag-5806.

Frepoli, A., Amato, A., 1997. Contemporaneous extension and compression in the northern Apennines from earthquake fault-plane solutions. Geophys. J. Int. 129, 368-388, doi.

Galadini, F., Galli, P., 2000. Active Tectonics in the Central Apennines (Italy) - Input Data for Seismic Hazard Assessment. Natural Hazards 22, 225-270, doi.

Geist, E.L., Andrews, D.J., 2000. Slip rates on San Francisco Bay area faults from anelastic deformation of the continental lithosphere. Journal of Geophysical Research 105, 25543, doi: 10.1029/2000jb900254.

Ghisetti, F., Vezzani, L., 2002. Normal faulting, extension and uplift in the outer thrust belt of the central Apennines (Italy): role of the Caramanico fault. Basin Research 14, 225-236, doi.

Gold, R.D., Cowgill, E., Wang, X.-F., Chen, X.-H., 2006. Application of trishear fault-propagation folding to active reverse faults: examples from the Dalong Fault, Gansu Province, NW China. Journal of Structural Geology 28, 200-219, doi: 10.1016/j.jsg.2005.10.006.

Hardy, S., Ford, M., 1997. Numerical modeling of trishear fault propagation folding. Tectonics 16, 841-854, doi: 10.1029/97tc01171.

Herak, D., Herak, M., Prelogović, E., Markušić, S., Markulin, Ž., 2005. Jabuka island (Central Adriatic Sea) earthquakes of 2003. Tectonophysics 398, 167-180, doi: 10.1016/j.tecto.2005.01.007.

Hetland, E.A., Hager, B.H., 2006. Interseismic strain accumulation: Spin-up, cycle invariance, and irregular rupture sequences. Geochemistry, Geophysics, Geosystems 7, n/a-n/a, doi: 10.1029/2005gc001087.

Hsu, Y.-J., Simons, M., Yu, S.-B., Kuo, L.-C., Chen, H.-Y., 2003. A two-dimensional dislocation model for interseismic deformation of the Taiwan mountain belt. Earth and Planetary Science Letters 211, 287-294, doi: 10.1016/s0012-821x(03)00203-6.

Kastelic, V., Carafa, M.M.C., 2012. Fault slip rates for the active External Dinarides thrust-and-fold belt. Tectonics 31, n/a-n/a, doi: 10.1029/2011tc003022.

Maesano, F.E., D'Ambrogi, C., 2015. Coupling sedimentation and tectonic control: Pleistocene evolution of the central Po Basin. Italian Journal of Geosciences 135, 1-45, doi: 10.3301/ijg.2015.17.

Maesano, F.E., D'Ambrogi, C., Burrato, P., Toscani, G., 2015. Slip-rates of blind thrusts in slow deforming areas: Examples from the Po Plain (Italy). Tectonophysics 643, 8-25, doi: 10.1016/j.tecto.2014.12.007.

Maesano, F.E., Toscani, G., Burrato, P., Mirabella, F., D'Ambrogi, C., Basili, R., 2013. Deriving thrust fault slip rates from geological modeling: Examples from the Marche coastal and offshore contraction belt, Northern Apennines, Italy. Marine and Petroleum Geology 42, 122-134, doi: 10.1016/j.marpetgeo.2012.10.008.

Megna, A., Barba, S., Santini, S., 2005. Normal-fault stress and displacement through finite-element analysis. Annals of Geophysics 48, 1009-1016, doi.

Melosh, H.J., Raefsky, A., 1981. A simple and efficient method for introducing faults into finite element computations. Bulletin of the Seismological Society of America 71, 1391-1400, doi.

Michetti, A.M., Brunamonte, F., Serva, L., Vittori, E., 1996. Trench investigations of the 1915 Fucino earthquake fault scarp (Abruzzo, central Italy): geological evidence of large historical events. Journal of Geophysical Research 101, 5921-5936, doi: 10.1029/95JB02852.

Nadeau, R.M., 1999. Fault Slip Rates at Depth from Recurrence Intervals of Repeating Microearthquakes. Science 285, 718-721, doi: 10.1126/science.285.5428.718.

Negredo, A.M., Carminati, E., Barba, S., Sabadini, R., 1999. Dynamic modelling of stress accumulation in central Italy. Geophysical Research Letters 26, 1945-1948, doi: 10.1029/1999gl900408.

Pace, B., 2006. Layered Seismogenic Source Model and Probabilistic Seismic-Hazard Analyses in Central Italy. Bulletin of the Seismological Society of America 96, 107-132, doi: 10.1785/0120040231.

Pantosti, D., D'Addezio, G., Cinti, F.R., 1996. Paleoseismicity of the Ovindoli-Pezza fault,central Apennines, Italy: a history including a large, previously unrecorded earthquake in Middle Ages (886-1300 A.D.). Journal of Geophysical Research 101, 5937-5959, doi.

Papanikolaou, I.D., Roberts, G.P., Michetti, A.M., 2005. Fault scarps and deformation rates in Lazio–Abruzzo, Central Italy: Comparison between geological fault slip-rate and GPS data. Tectonophysics 408, 147-176, doi: 10.1016/j.tecto.2005.05.043.

Patacca, E., Scandone, P., Di Luzio, E., Cavinato, G.P., Parotto, M., 2008. Structural architecture of the central Apennines: Interpretation of the CROP 11 seismic profile from the Adriatic coast to the orographic divide. Tectonics 27, n/a-n/a, doi: 10.1029/2005tc001917.

Pizzi, A., Calamita, F., Coltorti, M., Pieruccini, P., 2002. Quaternary normal faults, intramontane basins and seismicity in the Umbria-Marche-Abruzzi Apennine Ridge (Italy):contribution of neotectonic analysis to seismic hazard assessment. Boll. Soc. Geol. It. Volume speciale n. 1, 923-929, doi.

Pollitz, F.F., Nyst, M., Nishimura, T., Thatcher, W., 2006. Inference of postseismic deformation mechanisms of the 1923 Kanto earthquake. Journal of Geophysical Research 111, doi: 10.1029/2005jb003901.

Pondrelli, S., Morelli, A., 2008. Seismic strain and stress field studies in Italy before and after the Umbria-Marche seismic sequence: a review. Annals of Geophysics 51, 319-330, doi.

Pondrelli, S., Salimbeni, S., Morelli, A., Ekström, G., Postpischl, L., Vannucci, G., Boschi, E., 2011. European–Mediterranean Regional Centroid Moment Tensor catalog: Solutions for 2005–2008. Physics of the Earth and Planetary Interiors 185, 74-81, doi: 10.1016/j.pepi.2011.01.007.

Riguzzi, F., Tertulliani, A., Gasparini, C., 1989. Study of the Seismic Sequence of Porto San Giorgio (Marche) - 3 July 1987. Il Nuovo Cimento 12, 453-465, doi.

Roberts, G.P., Cowie, P., Papanikolaou, I., Michetti, A.M., 2004. Fault scaling relationships, deformation rates and seismic hazards: an example from the Lazio–Abruzzo Apennines, central Italy. Journal of Structural Geology 26, 377-398, doi: 10.1016/s0191-8141(03)00104-4.

Rosenbaum, G., Lister, G.S., 2004. Neogene and Quaternary rollback evolution of the Tyrrhenian Sea, the Apennines, and the Sicilian Maghrebides. Tectonics 23, n/a-n/a, doi: 10.1029/2003tc001518.

Rovida, A., Camassi, R., Gasperini, P., Stucchi, M., (eds.), 2011. CPTI11, the 2011 version of the Parametric Catalogue of Italian Earthquakes. Istituto Nazionale di Geofisica e Vulcanologia Milano, Bologna, http://emidius.mi.ingv.it/CPTI, doi: 10.6092/INGV.IT-CPTI11.

Speranza, F., Minelli, L., 2014. Ultra-thick Triassic dolomites control the rupture behavior of the central Apennine seismicity: Evidence from magnetic modeling of the L'Aquila fault zone. Journal of Geophysical Research: Solid Earth 119, 6756-6770, doi: 10.1002/2014jb011199.

Tiberti, M.M., Orlando, L., Di Bucci, D., Bernabini, M., Parotto, M., 2005. Regional gravity anomaly map and crustal model of the Central–Southern Apennines (Italy). Journal of Geodynamics 40, 73-91, doi: 10.1016/j.jog.2005.07.014.

Tizzani, P., Castaldo, R., Solaro, G., Pepe, S., Bonano, M., Casu, F., Manunta, M., Manzo, M., Pepe, A., Samsonov, S., Lanari, R., Sansosti, E., 2013. New insights into the 2012 Emilia (Italy) seismic sequence through advanced numerical modeling of ground deformation InSAR measurements. Geophysical Research Letters 40, 1971-1977, doi: 10.1002/grl.50290.

Tozer, R.S.J., Butler, R.W.H., Corrado, S., 2002. Comparing thin- and thick-skinned thrust tectonic models of the Central Apennines, Italy. EGU Stephan Mueller Special Publication Series 1, 181–194, doi.

Trubienko, O., Fleitout, L., Garaud, J.-D., Vigny, C., 2013. Interpretation of interseismic deformations and the seismic cycle associated with large subduction earthquakes. Tectonophysics 589, 126-141, doi: 10.1016/j.tecto.2012.12.027.

Vannoli, P., Basili, R., Valensise, G., 2004. New geomorphologic evidence for anticlinal growth driven by blind-thrust faulting along the northern Marche coastal belt (central Italy). Journal of Seismology 8, 297-312, doi.

Vannoli, P., Vannucci, G., Bernardi, F., Palombo, B., Ferrari, G., 2015. The Source of the 30 October 1930 Mw 5.8 Senigallia (Central Italy) Earthquake: A Convergent Solution from Instrumental, Macroseismic, and Geological Data. Bulletin of the Seismological Society of America 105, 1548-1561, doi: 10.1785/0120140263.

Vergne, J., Cattin, V., Avouac, J.P., 2001. On the use of dislocations to model interseismic strain and stress build-up at intracontinental thrust faults. Geophys. J. Int. 147, 155-162, doi.

Visini, F., de Nardis, R., Lavecchia, G., 2010. Rates of active compressional deformation in central Italy and Sicily: evaluation of the seismic budget. International Journal of Earth Sciences 99, 243-264, doi: 10.1007/s00531-009-0473-x.

Wang, R., Lorenzo-Martín, F., Roth, F., 2006. PSGRN/PSCMP—a new code for calculating co- and post-seismic deformation, geoid and gravity changes based on the viscoelastic-gravitational dislocation theory. Computers & Geosciences 32, 527-541, doi: 10.1016/j.cageo.2005.08.006.

Ward, S.N., Valensise, G., 1996. Progressive growth of San Clemente Island, California, by blind thrust faulting: implications for fault slip partitioning in the California Continental Borderland. Geophys. J. Int. 126, 712-734, doi.

Figure captions

Figure 1. Map of the study area. The modelled faults are labelled by F1-F7. Normal faults: F1, Val Roveto; F2, Avezzano; F3, L'Aquila-Borbona; F4, Sulmona; F5, Caramanico. Thrust faults: F6, Citeriore deep; F7, Citeriore shallow. All faults are from DISS 3.2.0 (DISS Working Group, 2015), except for the traces of F1 and F5, which are from Tozer et al. (2002) and Ghisetti & Vezzani (2002), respectively. A-A' is the trace of the numerical model. The black dashed line represents the trace of the CROP11 seismic profile from Patacca et al. (2008). Historical earthquakes (years 1000-2006) are from CPTI11 (Rovida et al., 2011). The L'Aquila (2009-04-06) and Jabuka (2003-03-29) earthquakes are from Chiarabba et al. (2009) and Herak et al. (2005), respectively.

Figure 2. Stratigraphy (seven layers, S1-S7; see text for description) of the numerical model section (A-A'; see Figure 1 for location) with the embedded discontinuities (red lines), including seven faults (F1-F7) and two detachments on the Tyrrhenian side (DET) and Adriatic side (DAT). Note that the intersection between the Adriatic and Tyrrhenian Moho (ITAM) takes several positions between the marked endpoints (black and red open circles) in the model.

Figure 3. (a) Geodetic velocities (blue arrows) along with 1-sigma confidence error regions (blue ellipses) from Devoti et al. (2011) in central Italy. The rectangular selection region (dashed outline) for the reference GPS velocities (Figure 4) is shown. The colour shading approximately represents the deformation domains from the extension (red) to contraction (blue). Earthquake focal mechanisms (1997-2015) are from Pondrelli et al. (2011) except for those labelled by numbers: 1) Vannoli et al. (2015); 2) Riguzzi et al. (1989); 3-4) quick solutions of recent earthquakes downloaded from the INGV web portal (http://cnt.rm.ingv.it/event/6286861 and http://cnt.rm.ingv.it/event/6288651, respectively; last accessed 28/12/2015). Hachured red lines represent the main thrust fronts. (b) Schematic geological cross section (trace marked as F&F in the map) redrawn from Fantoni & Franciosi (2010) showing the west-dipping Apennines thrusts and the east-dipping Dinarides thrusts. The assumed geodetic zero velocity point (black arrow) is positioned at the face-off between the two thrust belts.

Figure 4. GPS-derived horizontal velocity: point data (diamonds) along with 1-sigma confidence error bars projected along the model section (A-A' in Figure 3) and filtered longitudinal velocity (thick black line) with 95% confidence interval (thin grey lines). The extent of the extensional, transitional, and contractional domains are shown (horizontal arrows; the dashed tail indicates indefinite arrow termination).

Figure 5. (a) Finite element mesh and boundary conditions. The rollers indicate that the model can be freely displaced parallel to the edge, whereas it is locked in the orthogonal direction (the edges are also deformable). The arrows along the lower long edge represent the basal shear traction (single headed) and

the slab rollback velocity (two-headed). (b) Close up view of the fault area showing the smaller elements around the fault planes. Layer and fault labels are the same as in Figure 2. The model section trace (A-A') is shown in Figure 1.

Figure 6. Horizontal velocity distribution along the model section from the best interseismic model (red line). The location of modelled faults (F1-F7) along the section is indicated (dashed lines). Other symbols are as in Figure 4.

Figure 7. (a) Average slip rate for the 16 fault combinations (see Figure 1 for the location of F1-F7). The bold dashed line highlights values from the configuration SR01. (b) Slip rate depth distribution for the configuration SR01 (black dashed lines) with uncertainties (grey-shaded area) derived by combining results from the five models with RMS deviation less than 0.1 (grey solid lines).

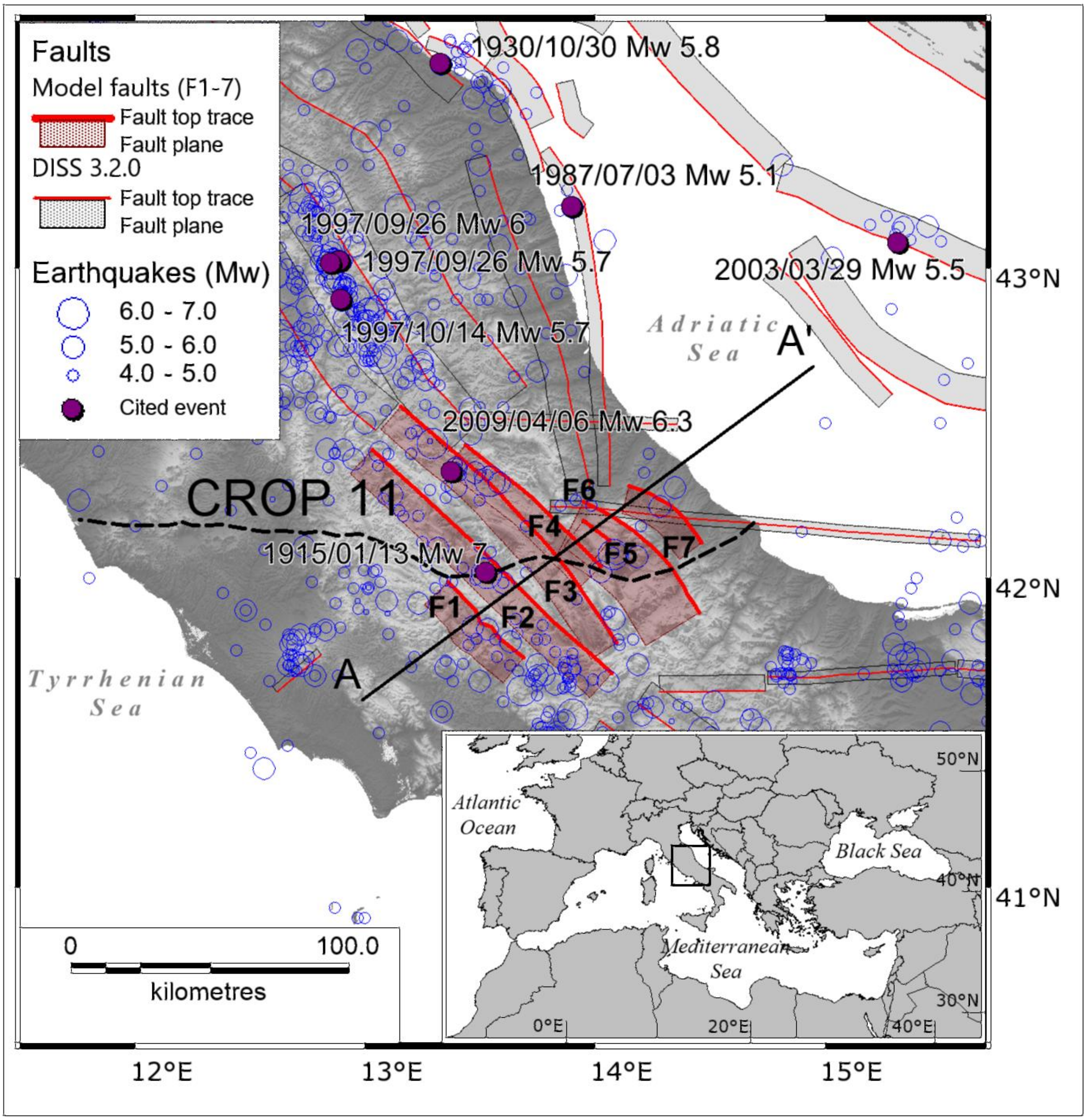

Figure 1. Map of the study area. The modelled faults are labelled by F1-F7. Normal faults: F1, Val Roveto; F2, Avezzano; F3, L'Aquila-Borbona; F4, Sulmona; F5, Caramanico. Thrust faults: F6, Citeriore deep; F7, Citeriore shallow. All faults are from DISS 3.2.0 (DISS Working Group, 2015), except for the traces of F1 and F5, which are from Tozer et al. (2002) and Ghisetti & Vezzani (2002), respectively. A-A' is the trace of the numerical model. The black dashed line represents the trace of the CROP11 seismic profile from Patacca et al. (2008). Historical earthquakes (years 1000-2006) are from CPTI11 (Rovida et al., 2011). The L'Aquila (2009-04-06) and Jabuka (2003-03-29) earthquakes are from Chiarabba et al. (2009) and Herak et al. (2005), respectively.

877

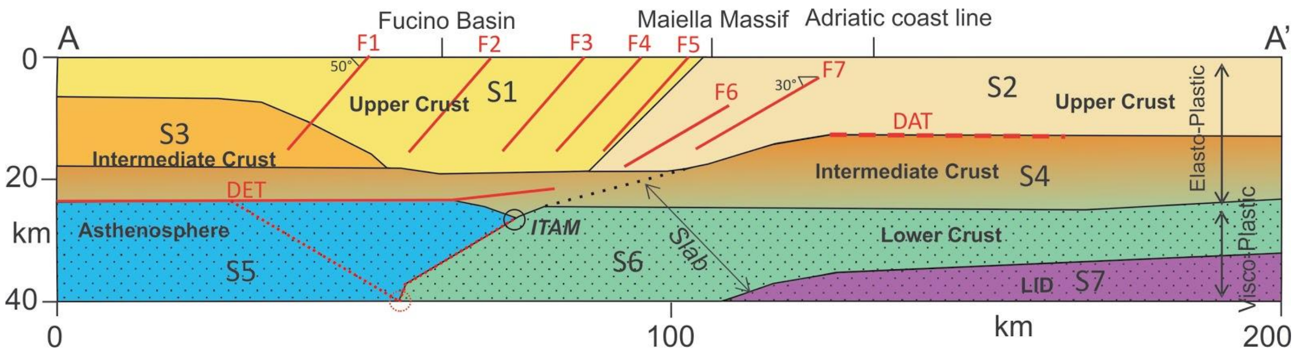

Figure 2. Stratigraphy (seven layers, S1-S7; see text for description) of the numerical model section (A-A'; see Figure 1 for location) with the embedded discontinuities (red lines), including seven faults (F1-F7) and two detachments on the Tyrrhenian side (DET) and Adriatic side (DAT). Note that the intersection between the Adriatic and Tyrrhenian Moho (ITAM) takes several positions between the marked endpoints (black and red open circles) in the model.

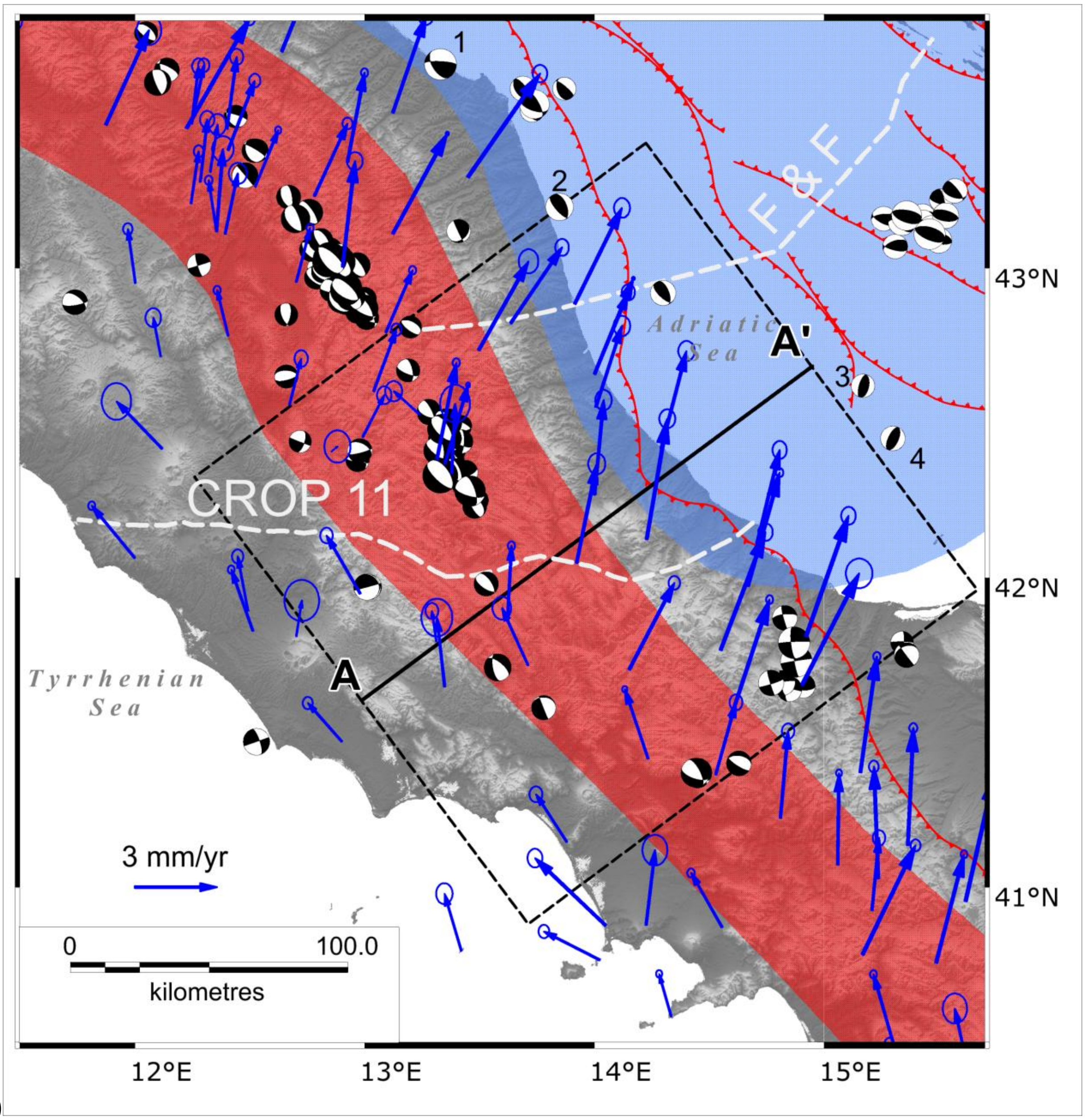

(a)

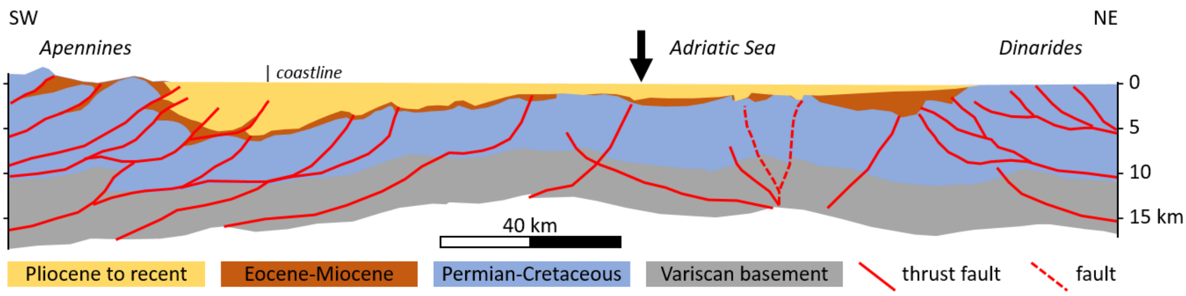

(b)

Figure 3. (a) Geodetic velocities (blue arrows) along with 1-sigma confidence error regions (blue ellipses) from Devoti et al. (2011) in central Italy. The rectangular selection region (dashed outline) for the reference GPS velocities (Figure 4) is shown. The colour shading approximately represents the deformation domains from the extension (red) to contraction (blue). Earthquake focal mechanisms (1997-2015) are from

Pondrelli et al. (2011) except for those labelled by numbers: 1) Vannoli et al. (2015); 2) Riguzzi et al. (1989); 3-4) quick solutions of recent earthquakes downloaded from the INGV web portal (http://cnt.rm.ingv.it/event/6286861 and http://cnt.rm.ingv.it/event/6288651, respectively; last accessed 28/12/2015). Hachured red lines represent the main thrust fronts. (b) Schematic geological cross section (trace marked as F&F in the map) redrawn from Fantoni & Franciosi (2010) showing the west-dipping Apennines thrusts and the east-dipping Dinarides thrusts. The assumed geodetic zero velocity point (black arrow) is positioned at the face-off between the two thrust belts.

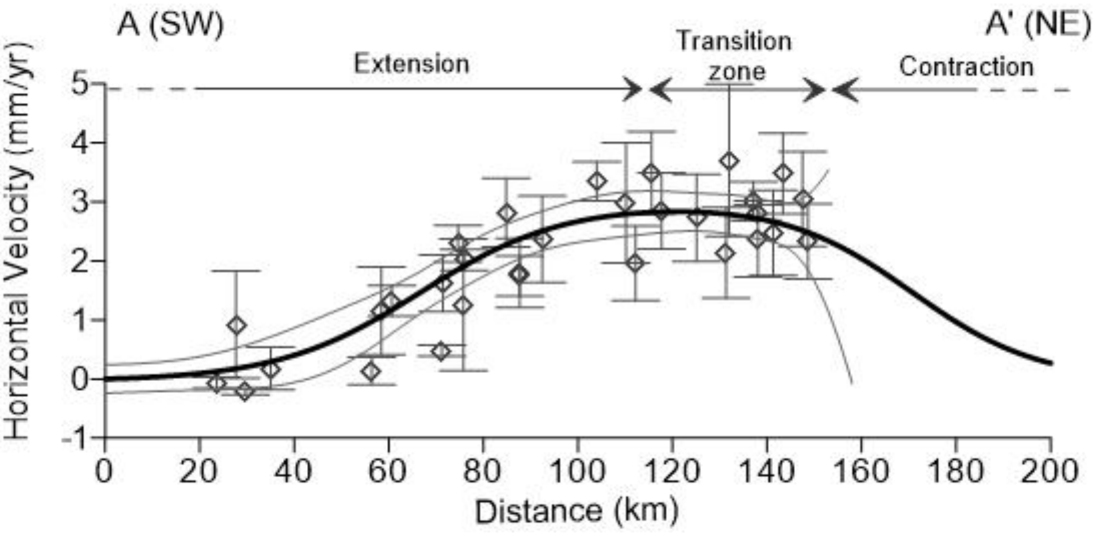

Figure 4. GPS-derived horizontal velocity: point data (diamonds) along with 1-sigma confidence error bars projected along the model section (A-A’ in Figure 3) and filtered longitudinal velocity (thick black line) with 95% confidence interval (thin grey lines). The extent of the extensional, transitional, and contractional domains are shown (horizontal arrows; the dashed tail indicates indefinite arrow termination).

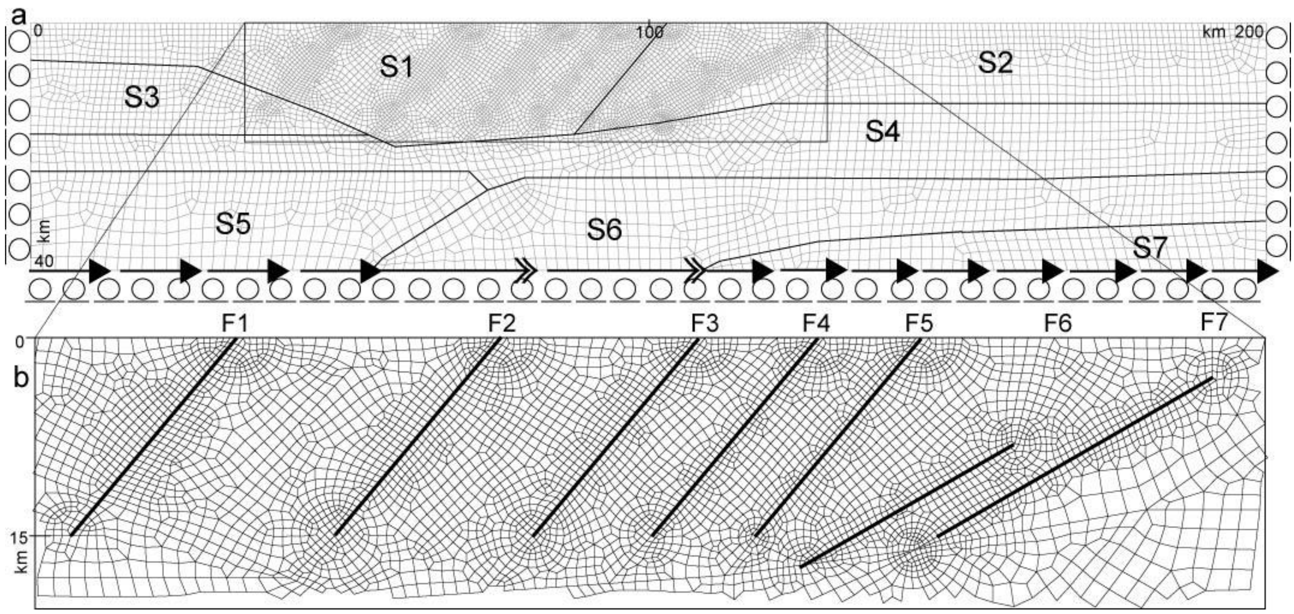

Figure 5. (a) Finite element mesh and boundary conditions. The rollers indicate that the model can be freely displaced parallel to the edge, whereas it is locked in the orthogonal direction (the edges are also deformable). The arrows along the lower long edge represent the basal shear traction (single headed) and the slab rollback velocity (two-headed). (b) Close up view of the fault area showing the smaller elements around the fault planes. Layer and fault labels are the same as in Figure 2. The model section trace (A-A’) is shown in Figure 1.

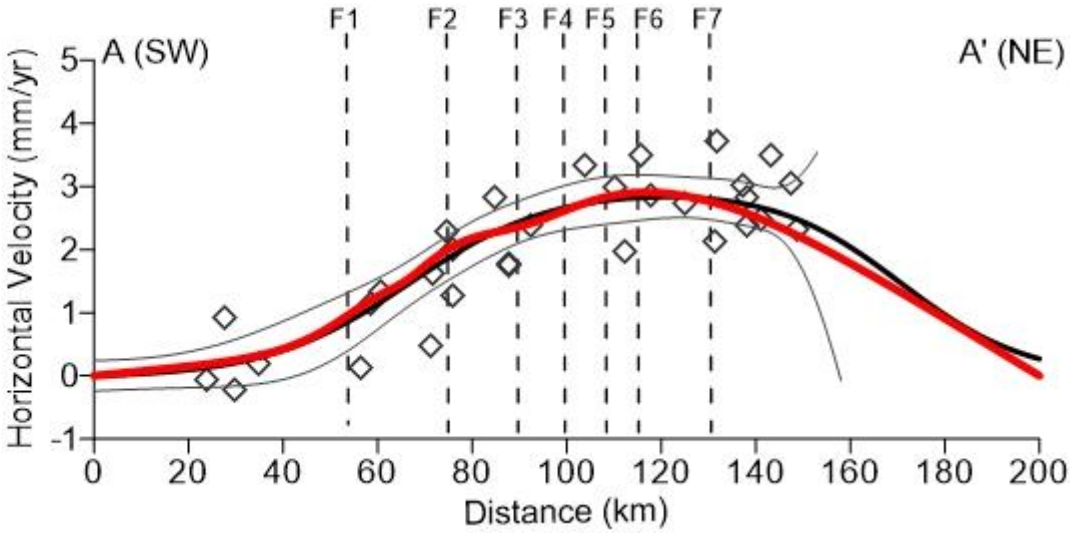

Figure 6. Horizontal velocity distribution along the model section from the best interseismic model (red line). The location of modelled faults (F1-F7) along the section is indicated (dashed lines). Other symbols are as in Figure 4.

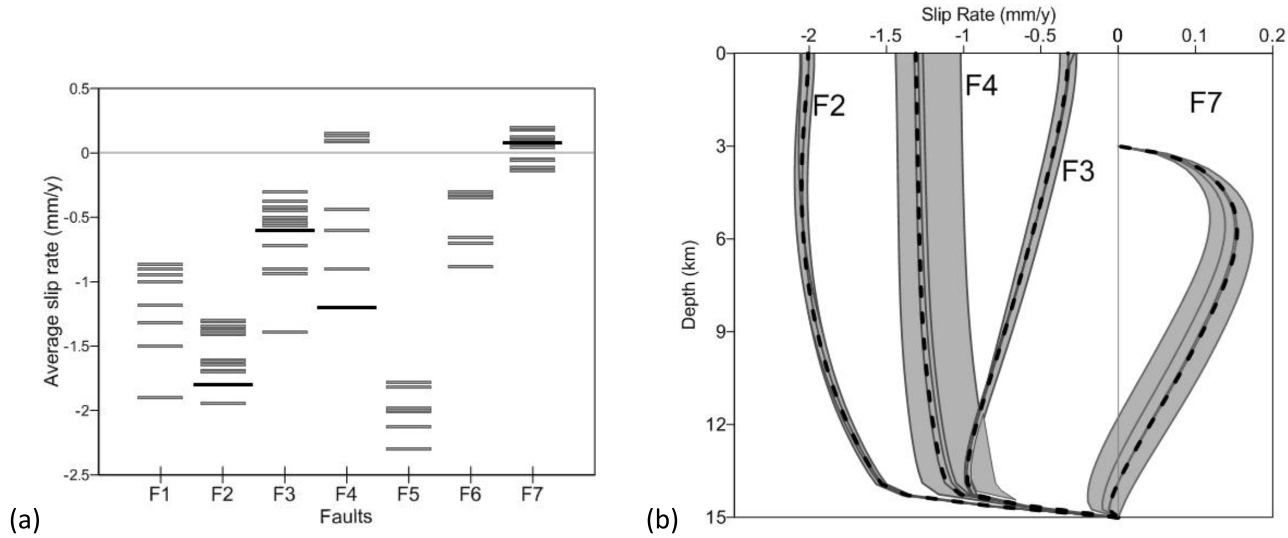

Figure 7. (a) Average slip rate for the 16 fault combinations (see Figure 1 for the location of F1-F7). The bold dashed line highlights values from the configuration SR01. (b) Slip rate depth distribution for the configuration SR01 (black dashed lines) with uncertainties (grey-shaded area) derived by combining results from the five models with RMS deviation less than 0.1 (grey solid lines).